




RESEARCH ARTICLE

WILEY

3D-MASNet: 3D mixed-scale asymmetric convolutional segmentation network for 6-month-old infant brain MR images

Zilong Zeng^{1,2,3} | Tengda Zhao^{1,2,3} | Lianglong Sun^{1,2,3} | Yihe Zhang^{1,2,3} |
 Mingrui Xia^{1,2,3}  | Xuhong Liao⁴ | Jiaying Zhang^{1,2,3} | Dinggang Shen^{5,6,7} |
 Li Wang⁸  | Yong He^{1,2,3,9} 

¹State Key Laboratory of Cognitive Neuroscience and Learning, Beijing Normal University, Beijing, China

²Beijing Key Laboratory of Brain Imaging and Connectomics, Beijing Normal University, Beijing, China

³IDG/McGovern Institute for Brain Research, Beijing Normal University, Beijing, China

⁴School of Systems Science, Beijing Normal University, Beijing, China

⁵School of Biomedical Engineering, ShanghaiTech University, Shanghai, China

⁶Shanghai Clinical Research and Trial Center, Shanghai, China

⁷Department of Research and Development, Shanghai United Imaging Intelligence Co., Ltd., Shanghai, China

⁸Department of Radiology and BRIC, University of North Carolina at Chapel Hill, Chapel Hill, North Carolina, USA

⁹Chinese Institute for Brain Research, Beijing, China

Correspondence

Tengda Zhao and Yong He, State Key Laboratory of Cognitive Neuroscience and Learning, Beijing Normal University, Beijing 100875, China.

Email: tengdazhao@bnu.edu.cn and yong.he@bnu.edu.cn

Funding information

National Natural Science Foundation of China, Grant/Award Numbers: 31830034, 81801783, 82021004; China Postdoctoral Science Foundation, Grant/Award Numbers: 2020TQ0050, 2022M710433; Changjiang Scholar Professorship Award, Grant/Award Number: T2015027

Abstract

Precise segmentation of infant brain magnetic resonance (MR) images into gray matter (GM), white matter (WM), and cerebrospinal fluid (CSF) are essential for studying neuroanatomical hallmarks of early brain development. However, for 6-month-old infants, the extremely low-intensity contrast caused by inherent myelination hinders accurate tissue segmentation. Existing convolutional neural networks (CNNs) based segmentation models for this task generally employ single-scale symmetric convolutions, which are inefficient for encoding the isointense tissue boundaries in baby brain images. Here, we propose a 3D mixed-scale asymmetric convolutional segmentation network (3D-MASNet) framework for brain MR images of 6-month-old infants. We replaced the traditional convolutional layer of an existing to-be-trained network with a 3D mixed-scale convolution block consisting of asymmetric kernels (MixACB) during the training phase and then equivalently converted it into the original network. Five canonical CNN segmentation models were evaluated using both T1- and T2-weighted images of 23 6-month-old infants from iSeg-2019 datasets, which contained manual labels as ground truth. MixACB significantly enhanced the average accuracy of all five models and obtained the most considerable improvement in the fully convolutional network model (CC-3D-FCN) and the highest performance in the Dense U-Net model. This approach further obtained Dice coefficient accuracies of 0.931, 0.912, and 0.961 in GM, WM, and CSF, respectively, ranking first among 30 teams on the validation dataset of the iSeg-2019 Grand Challenge. Thus, the proposed 3D-MASNet can improve the accuracy of existing CNNs-based segmentation models as a plug-and-play solution that offers a promising technique for future infant brain MRI studies.

KEYWORDS

convolutional neural networks, infant brain segmentation, mixed-scale convolution, MRI

This is an open access article under the terms of the [Creative Commons Attribution-NonCommercial](https://creativecommons.org/licenses/by-nc/4.0/) License, which permits use, distribution and reproduction in any medium, provided the original work is properly cited and is not used for commercial purposes.

© 2022 The Authors. *Human Brain Mapping* published by Wiley Periodicals LLC.

1 | INTRODUCTION

The accurate tissue segmentation of infant brain magnetic resonance (MR) images into gray matter (GM), white matter (WM), and cerebrospinal fluid (CSF) are essential for researchers to chart the normal and abnormal early brain development of cortical regions, white matter connections, and wiring topologies (Cao et al., 2017; Hazlett et al., 2017; Wang, Lian, et al., 2019; Wen et al., 2019; Xu et al., 2019; Zhao et al., 2019). Notably, the tissue segmentation of 6-month-old infants is the biggest challenge in baby brain segmentation tasks due to the isointense phase in which the intensity distributions of GM and WM voxels become dramatically overlapped in the cortical regions (Figure 1). The effective manual annotation, which is guided by longitudinal tracking of brain images with high tissue contrast in the latter children period (Wang, Nie, et al., 2019), is limited by the extremely high labor costs, the requirement of specialized expert knowledge (almost 1 week per image for an experienced neuroradiologist) and high inter- and intra-rater variations (Makropoulos et al., 2018). Developing fast, automatic, and accurate brain segmentation approaches is a crucial and ongoing goal for MR images of infants at 6 months of age (Sun et al., 2021; Wang, Nie, et al., 2019).

1.1 | Convolutional neural networks based methods become the mainstream

In the past years, many efforts have been made for the segmentation task of 6-month-old infant brain MR images. Generally, emerging convolutional neural networks (CNNs)-based segmentation methods that exhibiting faster computational speed and higher accuracy than conventional atlas-based (Wang et al., 2012, 2014) or machine learning based methods (Sanroma et al., 2018; Wang et al., 2014, 2015; Wang, Li, Adeli, et al., 2018) become the mainstream. A typical example is that seven of the eight top teams in iSeg-2017 challenge has utilized CNNs to segment infant brain tissues.

Current CNNs-based approaches for infant brain segmentation are usually variants of canonical FCN (Long et al., 2015) and U-Net (Ronneberger et al., 2015) architecture. By adjusting or adding specific

connectional pathways within or across neural layers on classical CNNs models, these approaches enhance the extraction and fusion of the semantic information in multimodal features to counteract the noisy and isointense tissues boundaries in 6-month-old infant brain images (Bui et al., 2019; Dolz et al., 2019, 2020; Nie et al., 2016, 2019; Wang et al., 2020; Wang, Li, Shi, et al., 2018; Zeng & Zheng, 2018; Zhang et al., 2015). Specifically, Bui et al. improved densely connected network (DenseNet) (Huang et al., 2017) by concatenating fine and coarse feature maps from multiple densely connected blocks and won the iSeg-2017 competition (Bui et al., 2019). Dolz et al. (2020) proposed a semi-dense network by directly connecting all of the convolutional layers to the end of the network and further extended it into a HyperDenseNet by adding dense connections between multimodal network paths (Dolz et al., 2019). Similarly, Zeng and Zheng (2018) modified the classical U-Net network by constructing multi-encoder paths for each modality to effectively extract targeted high-level information. Wang et al. (2020) designed a global aggregation block in the U-Net model to consider global information in the decoder path of feature maps. Interestingly, inspired by the superiority of DenseNet and U-Net, the densely connected U-Net (DU-Net) model with a combination of these two types of networks was proposed for both tissue segmentation and autism diagnosis (Wang, Li, Shi, et al., 2018).

1.2 | Improvements from fine-grained convolution kernel designs are underestimated

Although great efforts have been made, the above CNN-based segmentation models have several limitations. First, the image appearance of 6-month-old infant brain MR images is quite noisy (Li et al., 2019; Mostapha & Styner, 2019) which makes the effective feature extraction difficult for the traditional convolution kernel design in previous works. Adopting enhanced convolution kernel designs (Ding et al., 2019; Li et al., 2020; Zhang et al., 2022) that emphasizes key features in the skeleton center of kernels may facilitate feature extractions throughout the network. Second, the voxel-wise fuzzy tissue boundaries in infant brain images are constrained by

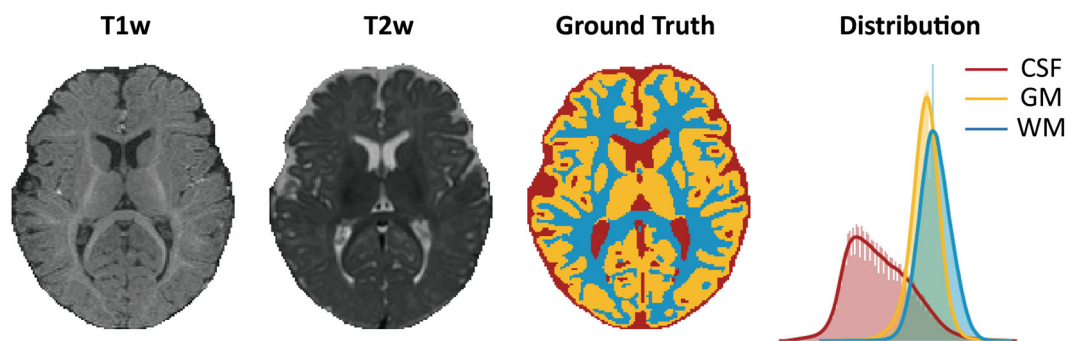


FIGURE 1 Data of a 6-month-old infant from the training set in iSeg-2019. The isointense brain appearance of an axial slice in T1-weighted (T1w) and T2-weighted (T2w) images. An axial view of the manual segmentation label (ground truth) and the corresponding brain tissue intensity distribution of the T1w image (distribution).

the anatomical morphology of gyrus at large spatial scales (Wang, Li, Adeli, et al., 2018). Although previous infant segmentation approaches try to fuse multi-scale features by skip-connections in variants of FCN and U-Net, they overlook capturing rich multi-scale features in kernel space, which contains more stable and homogeneous semantic information than features between layers (Fan et al., 2019). Third, all these studies focused on modifications of network layouts which need seasoned expertise experience, time-consuming hyperparameter tuning, and may also bring excessive graphics processing unit (GPU) burdens (Dolz et al., 2019; Wang et al., 2020) and architecture incompatibility. Recent CNN studies move eyes on building architecture-independent designs such as SE blocks (Hu et al., 2018), or automatically configuring models such as nnU-net (Isensee et al., 2021), which requires neither rare expert knowledge nor expensive manual interventions.

1.3 | Our contribution

Our goal is to obtain a CNN-based building block for 6-month-old infant brain image segmentation which is (1) with fine-grained kernel designs to enhance the representation and abundance of features; (2) transplantable in up-to-date segmentation models in a plug-and-play way; (3) without much additional hyperparameter tuning or computational burden. To this end, we construct a 3D mixed-scale asymmetric segmentation network (3D-MASNet) framework by embedding a well-designed 3D mixed-scale asymmetric convolution block (MixACB) into existing segmentation CNNs for 6-month-old infant brain MR images (Figure 2). The MixACB design is comprised by (1) four parallel 3D convolutional layers including a

symmetric kernel ($d \times d \times d$) and three asymmetric 2D kernels ($1 \times d \times d$, $d \times 1 \times d$, $d \times d \times 1$) (Figure 3a), respectively; (2) multiple groups on input feature maps with different kernel sizes (Figure 3b) independently; (3) parameter fusion for each MixACB after the training process to lower inference-time computations compare to the original network. We first evaluated the effectiveness of the MixACB on five canonical CNN networks using the iSeg-2019 training dataset. We next compared the performance of our method with that of top-4 approaches proposed in the MICCAI iSeg-2019 Grand Challenge on the iSeg-2019 validation dataset. The experimental results revealed that the MixACB significantly improved the segmentation accuracy of various CNNs, among which DU-Net (Wang, Li, Shi, et al., 2018) with MixACB achieved the best-enhanced average performance and obtained the highest Dice coefficients of 0.931 in GM, 0.912 in WM, and 0.961 in CSF, ranking first in the iSeg-2019 Grand Challenge. All codes are publicly available at <https://github.com/RicardoZiTseg/3D-MASNet>.

2 | METHODS AND IMPLEMENTATIONS

2.1 | Mathematical formulation of basic 3D convolution

Consider a feature map $I \in \mathbb{R}^{U \times V \times S \times C}$ with a spatial resolution of $U \times V \times S$ as input and a feature map $O \in \mathbb{R}^{R \times T \times Q \times K}$ with a spatial resolution of $R \times T \times Q$ as output of a convolutional layer with a kernel size of $H \times W \times D$ and K filters. Then, each filter's kernel is denoted as $F \in \mathbb{R}^{H \times W \times D \times C}$, and the operation of the convolutional layer with a batch normalization (BN) layer can be formulated as follows:

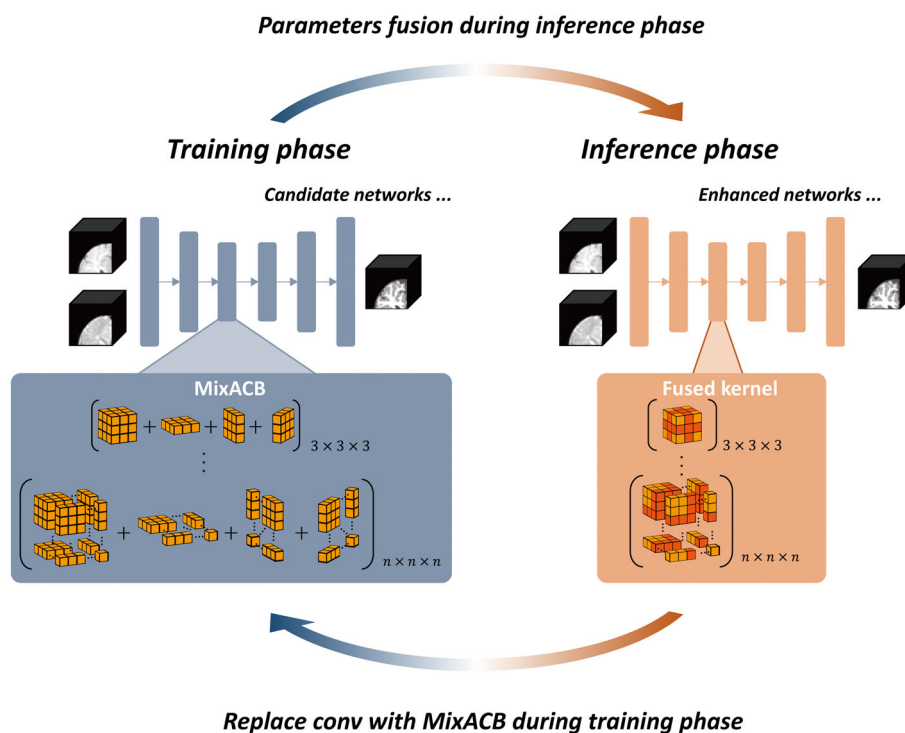


FIGURE 2 Overview of the 3D-MASNet framework. For a candidate network, we replace its traditional convolutional layers with MixACB during the training phase. Once the training process is complete, we fuse the parameters of MixACB to obtain an enhanced model containing fewer parameters after equivalent fusion.

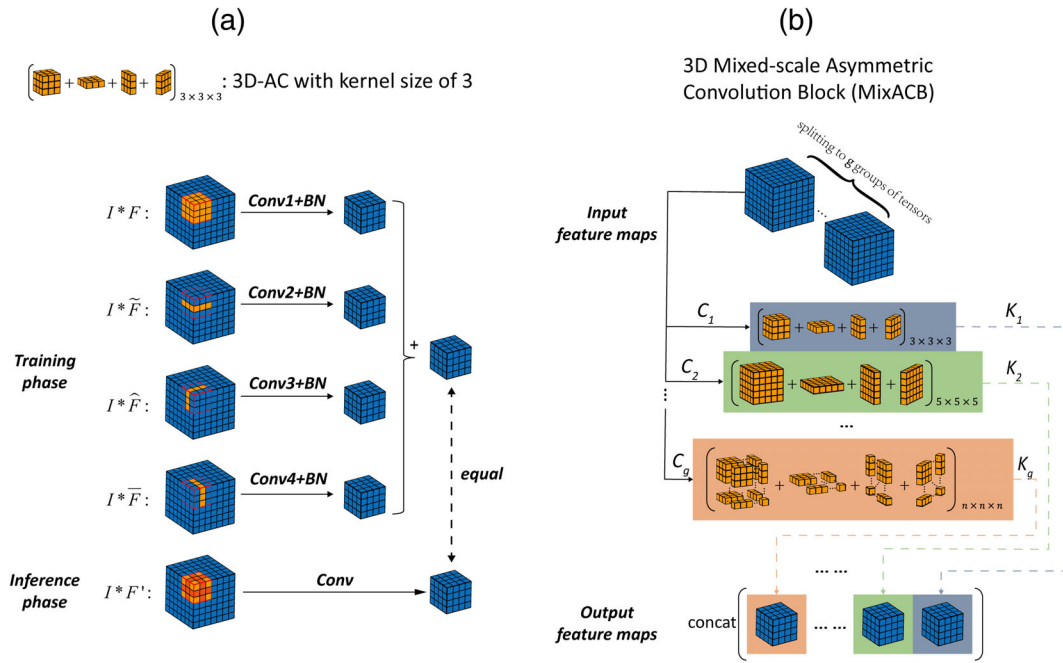


FIGURE 3 (a) Diagram of 3D-AC (taking a kernel size of 3 as an example), which has four convolutional layers during the training phase and one convolutional layer once kernel parameters have been fused during the inference phase. (b) Diagram of MixACB, which is composed of multiple 3D-ACs with different kernel sizes. MixACB splits input feature maps into several groups, applies asymmetric convolution on each group of feature maps, and then concatenates each group's output as the output feature maps.

$$\begin{aligned} O_{\dots,j} &= \left(\sum_{k=1}^C I_{\dots,k} * F_{\dots,k}^{(j)} - \mu_j \right) \cdot \frac{\gamma_j}{\sigma_j} + \beta_j \\ &= \left(\sum_{k=1}^C I_{\dots,k} * \frac{\gamma_j}{\sigma_j} F_{\dots,k}^{(j)} \right) - \frac{\mu_j \gamma_j}{\sigma_j} + \beta_j \end{aligned} \quad (1)$$

where $*$ is the 3D convolution operator, $I_{\dots,k}$ is the k^{th} channel of the input feature map I , $F_{\dots,k}^{(j)}$ is the k^{th} channel of the j^{th} filter's kernel, μ_j and σ_j are the channel-wise mean value and standard deviation value, respectively, γ_j and β_j are the scaling factor and bias term to restore the representation ability of the network, respectively.

2.2 | Design of 3D asymmetric convolutions (3D-AC) during training and inference phases

3D-AC was designed behaving differently during training and inference phases (Figure 3a). Concretely, for each kernel of each layer in the network during the training phase, a 3D-AC contains four parallel convolutional branches, namely one standard 3D convolution layer and three orthogonal 2D asymmetric convolutional layers ($1 \times d \times d$, $d \times 1 \times d$, $d \times d \times 1$) at kernel center for the enhancement of features along axial, sagittal, and coronal directions, respectively. The input feature maps are fed into these four branches, and the outputs of these branches are summed to fuse the knowledge learned by these four independent branches. During the inference phase, 3D-AC contains one standard convolutional layer with equivalently fused kernel of the training-time 3D-AC (described in Section 2.4), thus the input feature maps only need feed into this single branch which bringing low inference computations.

2.3 | Constructing MixACB by multiple 3D-ACs with varying kernel scales

To process the input feature map at different scales of detail, we propose the MixACB by mixing multiple 3D-ACs with different kernel sizes, as illustrated in Figure 3b. Notably, since we used the 3D-AC to strength the core skeleton part of the convolutional kernel, thus the kernel size of 3D-AC must be odd, such as 3, 5, and 7. Since directly adopting multiple 3D-ACs on all feature maps then concatenating outputs will dramatically increase the models' parameters and computations, we leverage the grouped convolution approach by splitting original input feature maps into groups and apply 3D-AC independently in each input feature map's group. Assume that we split the input feature maps into g groups of tensors such that their total number of channels is equal to the original feature maps' channels: $C_1 + C_2 + \dots + C_g = C$ with $C_1 \geq C_2 \geq \dots \geq C_g$; similarly, the output feature maps also have g groups: $K_1 + K_2 + \dots + K_g = K$ with $K_1 \geq K_2 \geq \dots \geq K_g$. We denote $I^{<i>} \in \mathbb{R}^{U \times V \times S \times C_i}$ as the i^{th} group of input, $\hat{O}^{<i>} \in \mathbb{R}^{R \times T \times Q \times K_i}$ as the MixACB's i^{th} group output, and $F'^{<i>} \in \mathbb{R}^{H_i \times W_i \times D_i \times C_i}$ as the equivalent kernel of the i^{th} group of the 3D-AC whose equivalent kernel size is $H_i \times W_i \times D_i$. Thus, we have following equations:

$$\begin{aligned} \hat{O}_{\dots,j}^{<i>} &= \left(\sum_{q=1}^{C_i} I_{\dots,q}^{<i>} * F_s'^{<i> (j)} \right) + b_j'^{<i>} \\ &\text{s.t. } 1 \leq i \leq g, 1 \leq j \leq K_i \end{aligned} \quad (2)$$

The final output of MixACB is the concatenation of all groups' outputs:

$$\bar{O} = \text{concat}\left(\bar{O}^{<1>}, \bar{O}^{<2>}, \dots, \bar{O}^{<g>}\right) \quad (3)$$

We define the mix ratio $mr_{1,i}$ as the ratio between C_1 and $C_i (1 < i \leq g)$. For simplicity, the ratio between K_1 and $K_i (1 < i \leq g)$ should be set to be equal to the $mr_{1,i}$, let $mr_{1,2} = mr_{1,3} = \dots = mr_{1,g}$, and the kernel size of the i^{th} group of 3D-AC as $2i + 1$. In this study, we particularly split the input and out feature maps into two groups, and set mix ratio $mr_{1,i}$ as 3:1. In Section 3.3.3, we further discussed the choice of group number g and mix ratio $mr_{1,i}$.

2.4 | Equivalently fusing kernel of each 3D-AC inside MixACB

Once the training process of 3D-MASNet is completed, we equivalently fused the kernels of each 3D-AC inside the MixACB to retain the same output results as the original network. Due to the additivity of convolutional kernels, the kernels of 3D-AC's four branches can be fused to obtain an equivalent kernel in a 3D convolutional layer to produce the same output, which can be formulated as the following equation:

$$I * F + I * \tilde{F} + I * \hat{F} + I * \bar{F} = I * \left(F \oplus \tilde{F} \oplus \hat{F} \oplus \bar{F}\right) \quad (4)$$

where I is an input feature map, F , \tilde{F} , \hat{F} , and \bar{F} are the four branches' kernels of 3D-AC. \oplus is an elementwise operator that performs parameter addition on the corresponding positions, and F' is the equivalent fused kernel of the four branches' kernels.

Here, we took a kernel size of 3 as an example. We first fused the BN parameters into the convolutional kernel term and bias term

following Equation (1). Then, we further fused the four parallel kernels by adding the asymmetric kernels onto the skeletons of the cubic kernel. Formally, we denote $F^{(j)}$ as the j^{th} filter at the $1 \times 3 \times 3$, $3 \times 1 \times 3$ and $3 \times 3 \times 1$ layer, respectively. Hence, we obtain the following formulas:

$$F^{(j)} = \frac{\tilde{\gamma}_j}{\sigma_j} F^{(j)} \oplus \frac{\tilde{\gamma}_j}{\tilde{\sigma}_j} \tilde{F}^{(j)} \oplus \frac{\hat{\gamma}_j}{\hat{\sigma}_j} \hat{F}^{(j)} \oplus \frac{\bar{\gamma}_j}{\bar{\sigma}_j} \bar{F}^{(j)} \quad (5)$$

$$b'_j = -\frac{\mu_j \tilde{\gamma}_j}{\sigma_j} - \frac{\tilde{\mu}_j \tilde{\gamma}_j}{\tilde{\sigma}_j} - \frac{\hat{\mu}_j \hat{\gamma}_j}{\hat{\sigma}_j} - \frac{\bar{\mu}_j \bar{\gamma}_j}{\bar{\sigma}_j} + \beta_j + \tilde{\beta}_j + \hat{\beta}_j + \bar{\beta}_j \quad (6)$$

Then, we can write any output of j^{th} filter as:

$$O_{\dots,j} + \tilde{O}_{\dots,j} + \hat{O}_{\dots,j} + \bar{O}_{\dots,j} = \sum_{k=1}^C I_{\dots,k} * F'_{\dots,k} + b'_j \quad (7)$$

where $O_{\dots,j}$, $\tilde{O}_{\dots,j}$, $\hat{O}_{\dots,j}$ and $\bar{O}_{\dots,j}$ are the outputs of the original $3 \times 3 \times 3$, $1 \times 3 \times 3$, $3 \times 1 \times 3$, and $3 \times 3 \times 1$ branch, respectively.

2.5 | Candidate CNNs for the evaluation of the MixACB on 6-month-old infant brain image segmentation

We choose five representative networks to evaluate the effectiveness of the 3D-MixACB in improving the segmentation performance, including BuiNet (Bui et al., 2019), 3D-UNet (Çiçek et al., 2016), convolution and concatenate 3D fully convolutional network (CC-3D-FCN) (Nie et al., 2019), non-local U-Net (NLU-Net) (Wang et al., 2020), and DU-Net (Wang, Li, Shi, et al., 2018).

TABLE 1 Training strategy of each candidate network

Candidate network	Training batch size	Training/inference patch size	Learning rate schedule
BuiNet	4	64	Train for 20,000 iterations. The initial learning rate is set to 2×10^{-4} and is decreased by a factor of 0.1 every 5000 iterations.
3D-UNet	10	32	Train for 80 epochs for a total of 5000 patches that are randomly extracted per epoch. The learning rate is decreased every 20 epochs and is set to 3×10^{-4} , 1×10^{-4} , 1×10^{-5} , and 1×10^{-6} . Train for 80 epochs for a total of 5000 patches that are randomly extracted per epoch. The learning rate is decreased every 20 epochs and is set to 3×10^{-4} , 1×10^{-4} , 1×10^{-5} , and 1×10^{-6} .
CC-3D-FCN	10	32	The same as 3D-UNet.
NLU-Net	5	32	Train for 80 epochs for a total of 5000 patches that are randomly extracted per epoch. The learning rate is set to 1×10^{-3} .
DU-Net	16	32	The cosine annealing strategy with a maximum learning rate of 3×10^{-4} and a minimum learning rate of 1×10^{-6} is adopted. The model is trained for 500 epochs and a total of 1000 patches are randomly extracted at each epoch.

Notably, these five networks are either variants of the U-type architecture (3D U-Net, NLU-Net, and DU-Net) or the FCN-type architecture (BuiNet and CC-3D-FCN) and encompass major CNN frameworks in infant brain segmentation. After replacing their original convolution layers with the 3D-MixACB design, we followed the training configurations set in the candidate CNN's release codes (Table 1) and adopted the Adam optimizer to update these models' parameters. Except for the CC-3D-FCN, which used the Xavier algorithm (Glorot & Bengio, 2010) to initialize network weights, all other networks adopted the He initialization method (He et al., 2015). The configuration parameters are as follows:

(1) BuiNet adopted four dense blocks consisting of four $3 \times 3 \times 3$ convolutional layers for feature extraction. Transition blocks were applied between every two dense blocks to reduce the feature map resolutions. 3D up-sampling operations were used after each dense block for feature map recovery, and these upsampled features were concatenated together. (2) 3D-UNet has four levels of resolution, and each level adopts one $3 \times 3 \times 3$ convolution, which is followed by BN and a rectified linear unit (ReLU). The $2 \times 2 \times 2$ max pooling and the $2 \times 2 \times 2$ transposed convolution, each with a stride of 2, are employed for resolution reduction and recovery. Feature maps of the same level of both paths were summed. (3) CC-3D-FCN used six groups of $3 \times 3 \times 3$ convolutional layers for feature extraction, in which the $2 \times 2 \times 2$ max pooling with a stride of 2 was adopted between two groups of layers. The $1 \times 1 \times 1$ convolution with a stride of 1 was added between two groups with the same resolution for feature fusion. (4) DU-Net used seven dense blocks to construct the encoder-decoder structure with four levels of resolution and leveraged transition down blocks and transition up blocks for down-sampling and up-sampling, respectively. Unlike the implementations in (Wang, Li, Shi, et al., 2018), the bottleneck layer is introduced into the dense block to constrain the rapidly increasing number of feature maps, and the transition down block consisted of two $3 \times 3 \times 3$ convolutions, each followed by BN and ReLU. In addition, we used the $1 \times 1 \times 1$ convolution followed by a softmax activation function in the last layer. (5) NLU-Net leveraged five different kinds of residual blocks to form the U-type architecture with three levels of resolution. BN with the ReLU6 activation function was adopted before each $3 \times 3 \times 3$ convolution. The global aggregation block replaced the two convolutional layers of the input residual block to form the bottom residual block for the integration of global information.

We fed the same multimodal images into these five networks and employed the same inference strategy. We extracted overlapping patches of the same size as that used during the training phase. The overlapping step size had to be smaller than or equal to the patch length size to form the whole volume. Following the common practice in (Bui et al., 2019; Nie et al., 2019; Wang et al., 2020; Wang, Li, Shi, et al., 2018), we set the step size to 8. Since the effect of the overlapping step size in the proposed framework remains unknown, we further evaluated it in Section 3.3. Voxels inside the overlapping regions were averaged.

3 | EXPERIMENTS AND RESULTS

3.1 | iSeg-2019 dataset and image preprocessing

Twenty-three isointense phase infant brain MRIs, including T1w and T2w images, were offered by the iSeg-2019 (<http://iseg2019.web.unc.edu/>) organizers from the pilot study of the Baby Connectome Project (BCP) (Howell et al., 2019). All the infants were term-born (40 ± 1 weeks of gestational age) with an average scan age of 6.0 ± 0.5 months. All experimental procedures were approved by the University of North Carolina at Chapel Hill and the University of Minnesota Institutional Review Boards. Detailed imaging parameters and preprocessing steps that were implemented are listed in (Sun et al., 2021). Before cropping the MR images into patches, we normalized the T1w and T2w images by subtracting the mean value and dividing by the standard deviation value.

The iSeg-2019 organizers offered the ground truth labels, which were obtained by a combination of initial automatic segmentation using the infant brain extraction and analysis toolbox (iBEAT) (Dai et al., 2013) on follow-up 24-month scans of the same baby and manual editing using ITK-SNAP (Yushkevich et al., 2006) under the guidance of an experienced neuroradiologist. The MR images of 10 infants with manual labels were provided for model training and validation. The images of 13 infants without labels were provided for model testing. The testing results were submitted to the iSeg-2019 organizers for quantitative measurements.

3.2 | Evaluation metrics

We employed the Dice coefficient (DICE), modified Hausdorff distance (MHD), and average surface distance (ASD) to evaluate the model performance on segmenting 6-month-old infant brain MR images.

3.2.1 | Dice coefficient

Let A and B be the manual labels and predictive labels, respectively. The DICE can be defined as:

$$DICE(A, B) = \frac{2|A \cap B|}{|A| + |B|} \quad (8)$$

where $|\cdot|$ denotes the number of elements of a point set. A higher DICE indicates a larger overlap between the manual and predictive segmentation areas.

3.2.2 | Modified Hausdorff distance

Let C and D be the sets of voxels within the manual and predictive segmentation boundary, respectively. MHD can be defined as:

$$\text{MHD}(C, D) = \max\{h(C, D), h(D, C)\} \quad (9)$$

where $h(C, D) = \frac{1}{N_c} \sum_{c \in C} d(c, D)$, and $d(c, D) = \min_{d \in D} \|c - d\|$ with $\|\cdot\|$ representing the Euclidean distance. We follow the calculation described in Wang et al. (2020) by computing the average MHD based on the three different vectorization directions to obtain a direction-independent evaluation metric. A smaller MHD coefficient indicates greater similarity between manual and predictive segmentation contours.

3.2.3 | Average surface distance

The ASD is defined as:

$$\text{ASD}(C, D) = \frac{1}{2} \cdot \left(\frac{\sum_{v_i \in S_C} \min_{v_j \in S_D} \|v_i - v_j\|}{\sum_{v_i \in S_C} 1} + \frac{\sum_{v_j \in S_D} \min_{v_i \in S_C} \|v_j - v_i\|}{\sum_{v_j \in S_D} 1} \right) \quad (10)$$

where S_C and S_D represent the surface meshes of C and D , respectively. A smaller ASD coefficient indicates greater similarity between cortical surfaces reconstructed from manual and predictive segmentation maps.

3.3 | Exploring the effectiveness of the MixACB

We performed several experiments to evaluate the effectiveness of the MixACB, including (1) ablation tests on five representative segmentation networks (Section 2.2); (2) comparisons with state-of-the-art approaches in iSeg-2019; (3) component analysis of MixACB and rotation simulation tests; (4) validation of the impact of the overlapping step size; and (5) investigating the numeric values of MixACB's kernels and visualizing feature maps.

3.3.1 | Performance improvement on five representative CNN architectures

For a given network architecture without the MixACB design, we regarded it as the baseline model and further transformed it into a

3D-MASNet design. All pairs of the baseline models and their corresponding 3D-MASNet followed the training strategies described in Table 1. To balance the training and testing sample sizes, we adopt a two-fold cross-validation (one fold with five random selected participants for training and the left for testing) for model evaluation on the iSeg-2019 training dataset. Tables 2 3 and Figure 4 show that the performance of all the models was significantly improved across almost all tissue types in terms of the DICE and MHD, which demonstrates the effectiveness of the MixACB on a wide range of CNN layouts. Specifically, DU-Net with the MixACB achieved the highest average DICE of 0.928 and the lowest average MHD value of 0.436; CC-3D-FCN with the MixACB gained the most considerable DICE improvement and reached a higher average DICE than that attained by BuiNet, which was a champion solution in the MIC-CAI iSeg-2017 grand challenge, indicating that a simple network could reach excellent performance by advanced convolution designs. Figure 5 further provides a visual segmentation comparison between networks with and without the MixACB. The MixACB could effectively correct misclassified voxels which are indicated by red squares.

3.3.2 | Comparison with state-of-the-art methods on iSeg-2019

Since DU-Net, which was combined with MixACB, has achieved the highest accuracy among all candidate models, we compared it with methods developed by the 29 remaining teams that participated in the iSeg-2019 challenge. We employed a majority-voting strategy on 10 trained networks' outputs to improve the model generalization.

Table 4 reports the segmentation results achieved by our proposed method and those of other teams' methods that ranked in the top 4 on the validation dataset of the iSeg-2019. The mean DICE, MHD value, and ASD value are presented for CSF, GM, and WM, representatively. Compared with other teams, our method yielded the highest DICE and lowest ASD value for the three brain tissues in the validation test of iSeg-2019, with comparable MHD values. The superior average value of the three types of brain tissues also indicates that our method has the best overall performance.

TABLE 2 Ablation study performed by comparing the segmentation accuracy between different models and their corresponding 3D-MASNet in terms of DICE by two-fold cross validation

Network	CSF		GM		WM		Avg	
	Baseline	MixACB	Baseline	MixACB	Baseline	MixACB	Baseline	MixACB
BuiNet	0.938 ± 0.010	0.938 ± 0.011	0.905 ± 0.007	0.908* ± 0.007	0.888 ± 0.014	0.892* ± 0.013	0.910 ± 0.007	0.912* ± 0.007
3D-UNet	0.940 ± 0.010	0.942* ± 0.008	0.907 ± 0.007	0.909* ± 0.007	0.889 ± 0.014	0.892* ± 0.015	0.912 ± 0.007	0.914* ± 0.008
CC-3D-FCN	0.923 ± 0.010	0.942* ± 0.008	0.910 ± 0.006	0.911 ± 0.007	0.892 ± 0.013	0.894* ± 0.013	0.908 ± 0.006	0.915* ± 0.006
NLU-Net	0.947 ± 0.009	0.949* ± 0.008	0.918 ± 0.007	0.919 ± 0.006	0.903 ± 0.012	0.904 ± 0.014	0.922 ± 0.006	0.924* ± 0.006
DU-Net	0.951 ± 0.008	0.953* ± 0.008	0.922 ± 0.007	0.923* ± 0.007	0.907 ± 0.015	0.907 ± 0.015	0.927 ± 0.007	0.928* ± 0.008

Note: The best values are highlighted in bold font. "Baseline" denotes that the corresponding model adopted the standard convolutional operation; "MixACB" denotes that the corresponding model was transformed into 3D-MASNet; "*" denotes that the difference between baseline and 3D-MASNet is statistically significant ($p < .05$).

TABLE 3 Ablation study performed by comparing the segmentation accuracy between different models and their corresponding 3D-MASNet in terms of MHD by two-fold cross validation

Network	CSF		GM		WM		Avg	
	Baseline	MixACB	Baseline	MixACB	Baseline	MixACB	Baseline	MixACB
BuiNet	0.308 ± 0.024	0.307 ± 0.023	0.659 ± 0.048	0.649* ± 0.045	0.493 ± 0.043	0.485* ± 0.042	0.487 ± 0.035	0.480* ± 0.034
3D-UNet	0.299 ± 0.022	0.293* ± 0.020	0.658 ± 0.050	0.651* ± 0.046	0.490 ± 0.046	0.485* ± 0.042	0.483 ± 0.036	0.476* ± 0.033
CC-3D-FCN	0.348 ± 0.022	0.292* ± 0.023	0.649 ± 0.047	0.645* ± 0.048	0.485 ± 0.046	0.480* ± 0.046	0.494 ± 0.034	0.473* ± 0.034
NLU-Net	0.278 ± 0.022	0.270* ± 0.020	0.619 ± 0.043	0.615* ± 0.040	0.461 ± 0.040	0.460 ± 0.037	0.453 ± 0.032	0.448* ± 0.030
DU-Net	0.261 ± 0.021	0.254* ± 0.022	0.605 ± 0.046	0.601* ± 0.047	0.452 ± 0.041	0.452 ± 0.043	0.439 ± 0.032	0.436* ± 0.034

Note: The best values are highlighted in bold font. “Baseline” denotes that the corresponding model adopted the standard convolutional operation; “MixACB” denotes that the corresponding model was transformed into 3D-MASNet; “*” denotes that the difference between baseline and 3D-MASNet is statistically significant ($p < .05$).

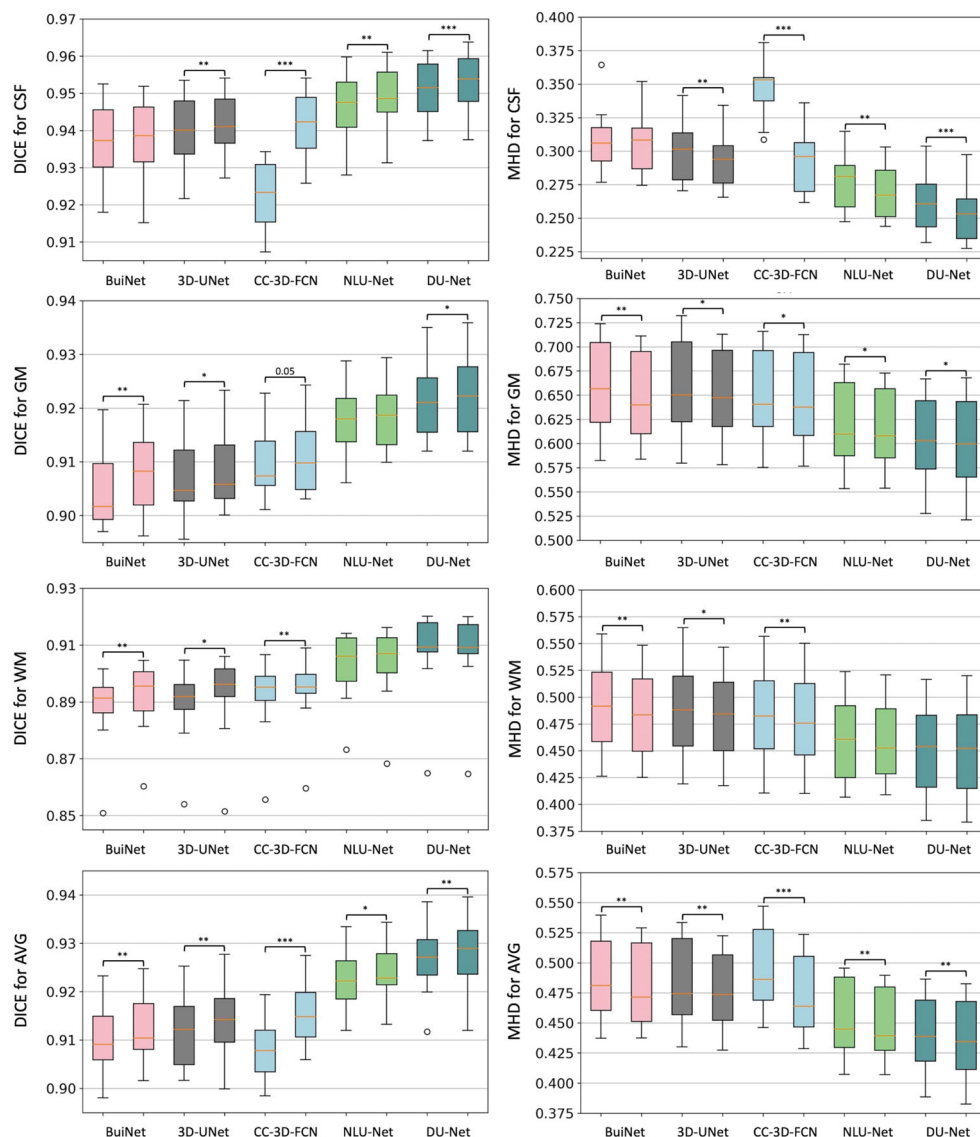


FIGURE 4 Box plot of the segmentation performance improvement on five candidate CNN architectures in the 3D-MASNet framework. The first column shows the measurement of DICE to represent the segmentation accuracy for each tissue type. The second column shows the results of MHD. In each subgraph, we use two neighbor box plots to represent a candidate model (first bar) and its corresponding 3D-MASNet (second bar). The significance of model comparison is evaluated by two-fold cross-validation. “***” denotes that $.01 \leq p < .05$, “**” denotes that $.001 \leq p < .01$, and “*” denotes that $p < .001$.

3.3.3 | Component analysis of MixACB and rotation simulation tests

To choose the group number g , we made an ablation experiment by gradually increasing g from 2 to 4. The maximum kernel size (which

was defined as $2g + 1$) varied from 5 to 7 and 9 and the kernel used varied from (3, 5) to (3, 5, 7) and (3, 5, 7, 9), respectively. For simplicity, the mix ratio of kernels with different lengths was set to an equal proportion. All other parameters were kept unchanged except that the number of parameters of model increased with the number and

FIGURE 5 Visualization of the segmentation results on different models with (w) and without (w/o) the MixACB. The ground truth map is shown in color, and CNNs-based segmentation maps are shown in the gray scale. The regions in the red square are magnified in the middle row following an order from with MixACB to without MixACB.

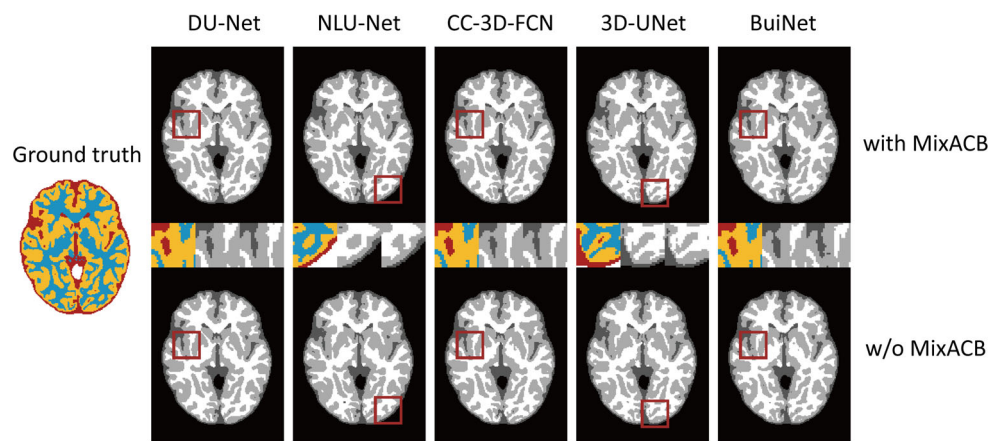


TABLE 4 Comparison of segmentation performance of the proposed method and the methods of the top-4 ranked teams on the 13 validation infant MRI images of iSeg-2019

Method (Top 5)	CSF			GM			WM			AVG		
	DICE	MHD	ASD	DICE	MHD	ASD	DICE	MHD	ASD	DICE	MHD	ASD
Brain_Tech	0.961	8.873	0.108	0.928	5.724	0.300	0.911	7.114	0.347	0.933	7.237	0.252
FightAutism	0.960	9.233	0.110	0.929	5.678	0.300	0.911	6.678	0.341	0.933	7.196	0.250
OxfordIBME	0.960	8.560	0.112	0.927	5.495	0.307	0.907	6.759	0.353	0.931	6.938	0.257
QL111111	0.959	9.484	0.114	0.926	5.601	0.307	0.908	7.028	0.353	0.931	7.371	0.258
Proposed	0.961	9.293	0.107	0.931	5.741	0.292	0.912	7.111	0.332	0.935	7.382	0.244

Note: The best values are highlighted in bold font.

size of kernels (Table 5). We found that with the increase of g , the segmentation accuracy was not improved. For facilitating multiple models' ensemble and reducing GPU memory usage, we set g as 2. Then we analyzed the effect of the mix ratio on model segmentation performance when g is set to 2. Table 6 shows that segmentation accuracy reaches the highest value when the mix ratio is set to 3:1. We next performed an ablation test to verify the effectiveness of each part of the proposed MixACB, as shown in Table 7. The segmentation accuracy was improved with large variations when using different 3D-ACs alone. Moreover, when these 3D-ACs were mixed in scales for a MixACB design, the model was able to achieve the best performance in both DICE and MHD metrics.

To explore the segmentation robustness of 3D-MASNet when facing residual rotation distortions, we conducted a simulation analysis by rotating the input brain images to a series of degrees in the testing set. Obviously, the accuracies were significantly reduced compared with that of non-rotation images (0°), but the network with MixACB presented higher accuracy than the baseline in most of rotation degrees (Table 8). This is consistent with previous findings that asymmetric convolutional designs are robust to image rotation distortions (Ding et al., 2019).

3.3.4 | Impact of overlapping step sizes

We further performed experiments to evaluate the effectiveness of the MixACB on overlapping step sizes, which controls the trade-off

between accuracy and inference time. Based on two-fold cross-validation, which has been done previously, we tested the overlapping impact when the step size is set to 4, 8, 16, and 32 on the DU-Net in the proposed 3D-MASNet framework. Figure 6a,b presents the changes in the segmentation performance in terms of DICE and MHD, respectively, for different overlapping step sizes. Figure 6c presents the changes in the average number of inference patches for different overlapping step sizes. We found that a step size of 8 is a reasonable choice for achieving fast and accurate results.

3.3.5 | Investigating the numeric values of MixACB's kernels and visualizing feature maps

Following the strategy described by Ding and colleagues (Ding et al., 2019), we calculated the average kernel magnitude matrix for DU-Net with MixACB and without MixACB to visualize the importance pattern of kernel parameters. We showed the magnitude matrix in Figure 7, where a darker color and a larger value at each grid indicated higher importance of the parameter in the corresponding position across all the convolutional layers. Similar to previous observations in (Ding et al., 2019), the parameters were distributed in an imbalanced manner in both with or without MixACB designs where the central part exhibited larger values than corner part (the second rows of Figure 7a,b). Meanwhile, MixACB aggravated such imbalance of parameter distribution (the first rows of Figure 7a,b). We also

TABLE 5 Ablation study performed by comparing the segmentation accuracy in different groups g by two-fold cross validation

g	CSF		GM		WM		AVG		Number of parameters
	DICE	MHD	DICE	MHD	DICE	MHD	DICE	MHD	
2	0.953 \pm 0.008	0.258 \pm 0.023	0.921 \pm 0.007	0.605 \pm 0.045	0.905 \pm 0.013	0.455 \pm 0.040	0.926 \pm 0.007	0.439 \pm 0.033	3,907,593
3	0.952 \pm 0.008	0.258 \pm 0.022	0.921 \pm 0.007	0.606 \pm 0.046	0.905 \pm 0.014	0.456 \pm 0.042	0.926 \pm 0.007	0.440 \pm 0.033	4,861,949
4	0.952 \pm 0.008	0.260 \pm 0.022	0.920 \pm .007	0.608 \pm 0.045	0.905 \pm 0.013	0.457 \pm 0.040	0.926 \pm 0.007	0.442 \pm 0.033	5,642,547

Note: The best values are highlighted in bold font.

TABLE 6 Ablation study performed by comparing the segmentation accuracy in different mix ratios with group $g = 2$ by two-fold cross validation

Mix ratio	CSF		GM		WM		AVG	
	DICE	MHD	DICE	MHD	DICE	MHD	DICE	MHD
1:0	0.952 \pm 0.010	0.261 \pm 0.024	0.922 \pm 0.008	0.604 \pm 0.045	0.906 \pm 0.014	0.453 \pm 0.041	0.927 \pm 0.008	0.440 \pm 0.033
1:1	0.953 \pm 0.008	0.258 \pm 0.023	0.921 \pm 0.007	0.605 \pm 0.045	0.905 \pm 0.013	0.455 \pm 0.040	0.926 \pm 0.007	0.439 \pm 0.033
3:1 (proposed)	0.953 \pm 0.008	0.254 \pm 0.022	0.923 \pm 0.007	0.601 \pm 0.047	0.907 \pm 0.015	0.452 \pm 0.043	0.928 \pm 0.008	0.436 \pm 0.034
5:1	0.953 \pm 0.009	0.257 \pm 0.025	0.922 \pm 0.008	0.601 \pm 0.047	0.907 \pm 0.015	0.452 \pm 0.042	0.926 \pm 0.008	0.437 \pm 0.034

Note: The best values are highlighted in bold font.

TABLE 7 Component analysis of MixACB by two-fold cross validation

	CSF		GM		WM		AVG	
	DICE	MHD	DICE	MHD	DICE	MHD	DICE	MHD
CONV_3	0.951 \pm 0.008	0.261 \pm 0.021	0.922 \pm 0.007	0.605 \pm 0.046	0.907 \pm 0.015	0.452 \pm 0.041	0.927 \pm 0.007	0.439 \pm 0.032
AC_3	0.952 \pm 0.010	0.261 \pm 0.024	0.922 \pm 0.008	0.604 \pm 0.045	0.906 \pm 0.014	0.453 \pm 0.041	0.927 \pm 0.008	0.440 \pm 0.033
CONV_5	0.947 \pm 0.012	0.276 \pm 0.023	0.918 \pm 0.008	0.619 \pm 0.047	0.903 \pm 0.016	0.463 \pm 0.043	0.922 \pm 0.008	0.453 \pm 0.034
AC_5	0.952 \pm 0.008	0.261 \pm 0.022	0.920 \pm 0.008	0.610 \pm 0.046	0.904 \pm 0.016	0.460 \pm 0.043	0.925 \pm 0.008	0.443 \pm 0.033
MixACB	0.953 \pm 0.008	0.254 \pm 0.022	0.923 \pm 0.007	0.601 \pm 0.047	0.907 \pm 0.015	0.452 \pm 0.043	0.928 \pm 0.008	0.436 \pm 0.034

Note: The best values are highlighted in bold font. "CONV_3" denotes that the 3D convolution with a kernel size of 3; "AC_3" denotes that the 3D-AC with a kernel size of 3; "CONV_5" denotes that the 3D convolution with a kernel size of 5; "AC_5" denotes that the 3D-AC with a kernel size of 5.

TABLE 8 The segmentation accuracy in terms of DICE with different rotation degrees between baseline (DU-Net) and the corresponding 3D-MASNet

Rotation degree	CSF		GM		WM		Avg	
	Baseline	MixACB	Baseline	MixACB	Baseline	MixACB	Baseline	MixACB
0°	0.951 \pm 0.008	0.953 \pm 0.008	0.922 \pm 0.007	0.923 \pm 0.007	0.907 \pm 0.015	0.907 \pm 0.015	0.927 \pm 0.007	0.928 \pm 0.008
15°	0.682 \pm 0.023	0.685 \pm 0.024	0.842 \pm 0.021	0.840 \pm 0.028	0.849 \pm 0.025	0.849 \pm 0.027	0.791 \pm 0.020	0.792 \pm 0.023
30°	0.678 \pm 0.024	0.683 \pm 0.024	0.831 \pm 0.022	0.830 \pm 0.030	0.837 \pm 0.026	0.837 \pm 0.027	0.782 \pm 0.021	0.783 \pm 0.024
45°	0.672 \pm 0.026	0.678 \pm 0.026	0.819 \pm 0.025	0.816 \pm 0.032	0.823 \pm 0.027	0.822 \pm 0.028	0.772 \pm 0.023	0.772 \pm 0.025

Note: The best values are highlighted in bold font.

visualized the feature maps produced from DU-Net with MixACB and without MixACB (Figure 8). We found that the feature maps with MixACB contained more meaningful response patterns and precise morphological details than those observed without MixACB (such as the 6th, 9th, and 14th maps).

4 | DISCUSSION

Instead of designing a new network architecture to segment the brain images of 6-month-old infants, we proposed a 3D-MASNet framework by replacing the standard convolutional layer with MixACB on

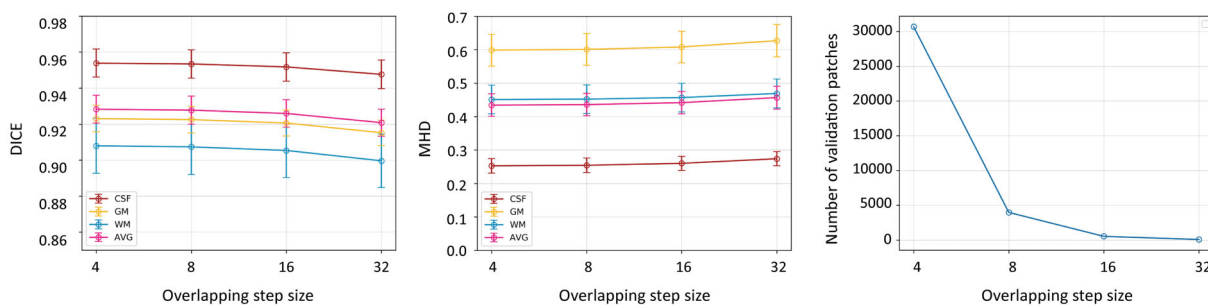
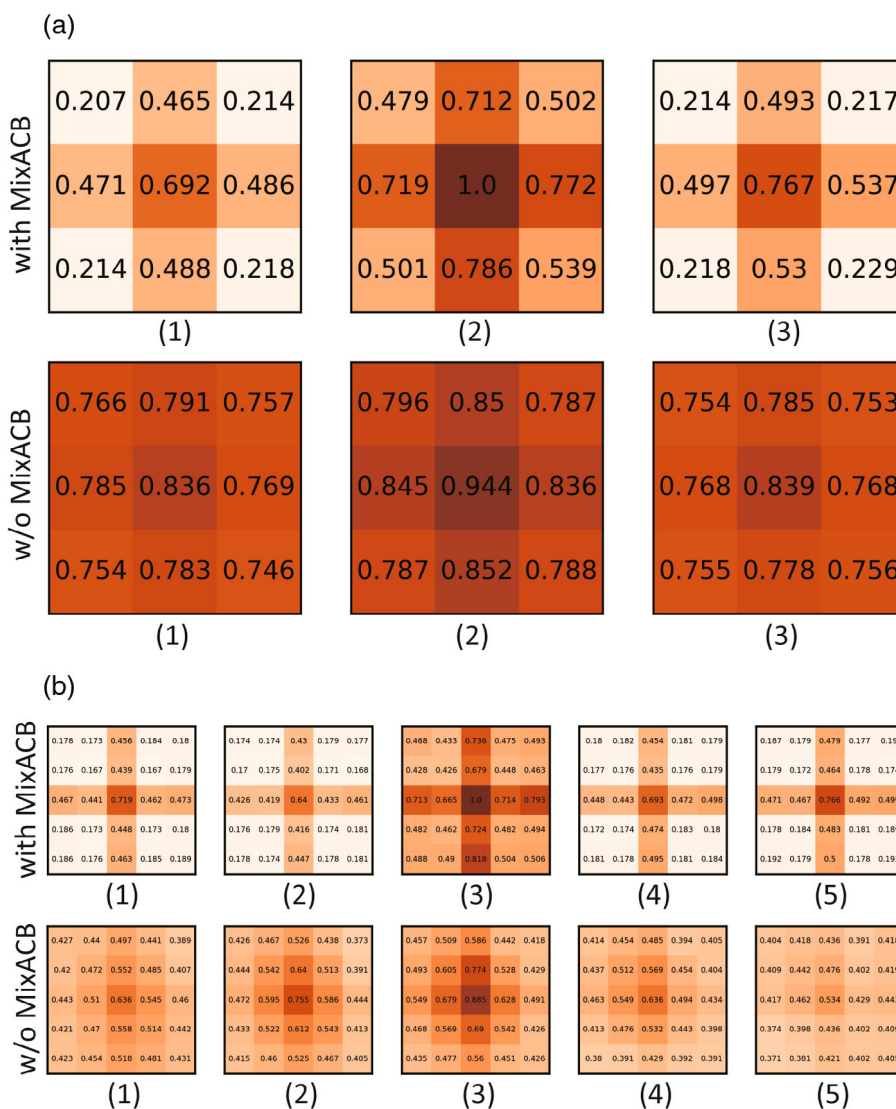


FIGURE 6 Changes in segmentation performance in terms of DICE (a) and MHD (b) with respect to different overlapping step sizes on 10 subjects during inference, where two-fold cross-validation is used. (c) Changes of the average number of the 10 subjects' patches with respect to different overlapping step sizes during inference.

FIGURE 7 We split the 3D convolutional kernels into multiple 2D slices for visualization. (a) The first and second rows are the average magnitude matrixes of kernel size of 3 for convolutional layer in MixACB and conventional convolutional layer, respectively. (b) The first and second rows indicate the average magnitude matrixes of kernel size of 5 for convolutional layer in MixACB and conventional convolutional layer, respectively.



an existing mature network and reduced model parameters and computations by equivalently performing fusion during the inference phase. The experimental results revealed that the MixACB significantly improved the performance of several CNNs by a considerable margin, in which DU-Net with MixACB showed the best average

segmentation accuracy. The proposed framework obtained the highest average DICE of 0.935 and lowest ASD of 0.244, which ranked first among all 30 teams on the validation dataset of the iSeg-2019 Grand Challenge. In addition, the CC-3D-FCN model showed the largest improvement, which indicates that a simple model could achieve

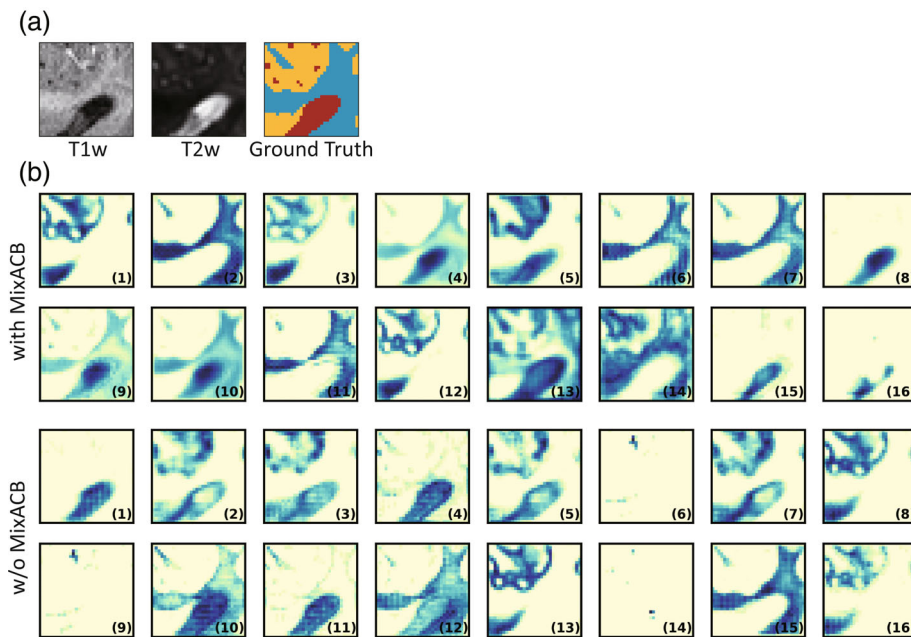


FIGURE 8 (a) The input patches (patch size = 32) of T1w image, T2w image, and corresponding ground truth segmentation label. (b) The entire 16 feature maps of DU-Net with MixACB and without (w/o) MixACB. The feature maps are the outputs of the last dense block of DU-Net. The number in the lower right corner of each feature map indicates the sequence number of the feature map.

relatively better performance by implementing our convolution design.

4.1 | Effectiveness of the MixACB on improving segmentation accuracy

The wide improvement in the segmentation accuracy of different models by the MixACB is derived from several aspects. First, the mixed-scale design of MixACB enables the network to collect multi-scale details of local features with different receptive fields, facilitating the integration of coarse-to-fine information inside the input patches at low-to-high semantic levels. Second, the isointense intensity distribution and heterogeneous tissue contrasts hamper effective feature extraction in baby brain images. The feature maps with multi-scale kernel size enriches small receptive fields with enough detail features while enabling large receptive fields for capturing coarse global features. We also employed the 3D-AC inside the MixACB by adding multiple orthogonal 3D asymmetric convolutional layers to emphasize informative feature patterns in the central place (Figure 3). Meanwhile, the asymmetric design showed robustness to image rotational distortions (Table 8), which can help the network to deal with the residual rotational differences of infant brain positions, even though these images have been linearly aligned to standard space. Third, the significant improvable performance of MixACB on various segmentation networks (Table 2, 3) indicates that inter-layer architecture design may not be sufficient for multi-scale information fusion. Notably, besides providing better performance than the previous networks, 3D-MASNet is also more efficient than the baseline models, requiring fewer model parameters once its parameters were fused in the inference phase. For example, the baseline DU-Net's number of parameters is 2,492,795, while the corresponding 3D-MASNet's number of

parameters is reduced from 3,117,549 to 2,341,141 after parameter fusion process during the inference phase. The average inference time was reduced from 110 to 57 s, without performance loss.

4.2 | Well-designed convolution operations

In recent years, researchers have begun to shift their interests from macro network layout to micro neuron units by studying specific convolution operators rather than touching the overall network. Previous works have proposed several advanced convolution operators by combining well-designed filters, such as pyramidal convolution (PyConv), dynamic group convolution (DGC), and asymmetric convolution block (ACB). PyConv employs multiple kernels in a pyramidal way to capture different levels of image details (Duta et al., 2020); DGC equips a feature selector for each group convolution conditioned on the input images to adaptively select input features (Su et al., 2020); ACB introduces asymmetry into 2D convolution to power up the representational power of the skeleton part of the kernel (Ding et al., 2019). Due to the “easy-to-plug-in” property, such convolutional designs could be conveniently adopted in various advanced CNNs and avoid high costs of network re-designing. Such implantations have achieved better performance or increased computational efficiency in natural image classification tasks (Ding et al., 2019; Duta et al., 2020; Su et al., 2020). Of note, none of these three methods has yet been applied on the infant brain MR image segmentation task. Due to blurred image appearance, large individual variation of brain morphology, and limited labeled sample sizes, we emphasize that effective and robust feature extraction by re-designing convolution kernels, especially in a plug-and-play form, is essential for the infant brain segmentation task. Therefore, we designed a novel 3D convolution block by combining two convolution

operations including asymmetry convolution (ACB) and mixed-scale kernels (pyramidal-like convolution designs). The effectiveness of ACB was shown in the ablation experiment in Table 7 (CONV_3 vs. AC_3, and CONV_5 vs. AC_5). The effectiveness of pyramidal-like kernel designs was shown in the ablation experiment in Tables 6 and 7 (1:0 vs. 3:1 in Table 6, MixACB vs. AC_3 and AC_5 in Table 7). As for the convolution operation of DGC, we only adopted a simple version by manually setting the mix ratio of convolution groups into several proportions and selecting the ratio with the highest segmentation accuracy (Table 6). Exhausting the combination of various convolution designs is an interesting topic, which is beyond the scope of the article and needs a future attention.

4.3 | Limitations and future directions

The current study has several limitations. First, the patching approach may cause spatial consistency loss near boundaries. Although we adopted a small overlapping step size to relieve this issue, it is necessary to consider further integrating guidance from global information. Second, the small sample sizes of infant-specific datasets limit the generalizability of our method for babies across MRI scanners and acquisition protocols. Further validation on large samples is needed. Third, image indexes, such as the fractional anisotropy derived from diffusion MRI, contain rich white matter information (Liu et al., 2007), which could be beneficial for insufficient tissue contrast (Nie et al., 2019; Zhang et al., 2015). Importantly, determining how to leverage mixed-scale asymmetric convolution to enhance specific model features needs to be further explored. Fourth, we only explored the effectiveness of MixACB when input feature maps are split into two to four groups. Further combination configurations of convolutional kernel sizes and mix ratios are warranted.

5 | CONCLUSION

In this paper, we proposed a 3D-MASNet framework for brain MR image segmentation of 6-month-old infants, which ranked first in the iSeg-2019 Grand Challenge. We demonstrated that the designed MixACB could easily migrate to various network architectures and enable performance improvement without extra inference-time computations. This work shows great adaptation potential for further improvement in future studies on brain segmentation.

ACKNOWLEDGMENTS

The study was supported by the National Natural Science Foundation of China (Nos. 31830034, 82021004, and 81801783), the China Postdoctoral Science Foundation (2020TQ0050 and 2022M710433), and the Changjiang Scholar Professorship Award (T2015027).

CONFLICT OF INTEREST

The authors have declared that there is no conflict of interest.

DATA AVAILABILITY STATEMENT

The 6-months-old infant brain MRI data were publicly offered by the iSeg-2019 (<http://iseg2019.web.unc.edu/>) organizers. Codes developed for the proposed segmentation algorithm are released at <https://github.com/RicardoZiTeng/3D-MASNet>.

ORCID

Mingrui Xia  <https://orcid.org/0000-0003-4615-9132>

Li Wang  <https://orcid.org/0000-0003-2165-0080>

Yong He  <https://orcid.org/0000-0002-7039-2850>

REFERENCES

- Bui, T. D., Shin, J., & Moon, T. (2019). Skip-connected 3D DenseNet for volumetric infant brain MRI segmentation. *Biomedical Signal Processing and Control*, 54, 101613.
- Cao, M., Huang, H., & He, Y. (2017). Developmental connectomics from infancy through early childhood. *Trends in Neurosciences*, 40, 494–506.
- Çiçek, Ö., Abdulkadir, A., Lienkamp, S. S., Brox, T., & Ronneberger, O. (2016). 3D U-Net: Learning dense volumetric segmentation from sparse annotation. *International conference on medical image computing and computer-assisted intervention*. Springer, pp. 424–432.
- Dai, Y., Shi, F., Wang, L., Wu, G., & Shen, D. (2013). iBEAT: A toolbox for infant brain magnetic resonance image processing. *Neuroinformatics*, 11, 211–225.
- Ding, X., Guo, Y., Ding, G., & Han, J. (2019). Acnet: Strengthening the kernel skeletons for powerful CNN via asymmetric convolution blocks. *Proceedings of the IEEE international conference on computer vision*, pp. 1911–1920.
- Dolz, J., Desrosiers, C., Wang, L., Yuan, J., Shen, D., & Ayed, I. B. (2020). Deep CNN ensembles and suggestive annotations for infant brain MRI segmentation. *Computerized Medical Imaging and Graphics*, 79, 101660.
- Dolz, J., Gopinath, K., Yuan, J., Lombaert, H., Desrosiers, C., & Ayed, I. B. (2019). HyperDense-Net: A hyper-densely connected CNN for multi-modal image segmentation. *IEEE Transactions on Medical Imaging*, 38, 1116–1126.
- Duta, I. C., Liu, L., Zhu, F., & Shao, L. (2020). Pyramidal convolution: Rethinking convolutional neural networks for visual recognition. *arXiv*. [Preprint] arXiv:2006.11538.
- Fan, J., Cao, X., Yap, P.-T., & Shen, D. (2019). BIRNet: Brain image registration using dual-supervised fully convolutional networks. *Medical Image Analysis*, 54, 193–206.
- Glorot, X., & Bengio, Y. (2010). Understanding the difficulty of training deep feedforward neural networks. *Proceedings of the thirteenth international conference on artificial intelligence and statistics. JMLR workshop and conference proceedings*, pp. 249–256.
- Hazlett, H. C., Gu, H., Munsell, B. C., Kim, S. H., Styner, M., Wolff, J. J., Elison, J. T., Swanson, M. R., Zhu, H., & Botteron, K. N. (2017). Early brain development in infants at high risk for autism spectrum disorder. *Nature*, 542, 348–351.
- He, K., Zhang, X., Ren, S., & Sun, J. (2015). Delving deep into rectifiers: Surpassing human-level performance on ImageNet classification. *2015 IEEE international conference on computer vision (ICCV)*, pp. 1026–1034.
- Howell, B. R., Styner, M. A., Gao, W., Yap, P.-T., Wang, L., Baluyot, K., Yacoub, E., Chen, G., Potts, T., & Salzwedel, A. (2019). The UNC/UMN baby connectome project (BCP): An overview of the study design and protocol development. *NeuroImage*, 185, 891–905.
- Hu, J., Shen, L., & Sun, G. (2018). Squeeze-and-excitation networks. *Proceedings of the IEEE conference on computer vision and pattern recognition*, pp. 7132–7141.
- Huang, G., Liu, Z., Van Der Maaten, L., & Weinberger, K. Q. (2017). Densely connected convolutional networks. *Proceedings of the IEEE conference on computer vision and pattern recognition*, pp. 4700–4708.

- Isensee, F., Jaeger, P. F., Kohl, S. A., Petersen, J., & Maier-Hein, K. H. (2021). nnU-Net: A self-configuring method for deep learning-based biomedical image segmentation. *Nature Methods*, 18, 203–211.
- Li, G., Wang, L., Yap, P. T., Wang, F., Wu, Z., Meng, Y., Dong, P., Kim, J., Shi, F., Rekić, I., Lin, W., & Shen, D. (2019). Computational neuroanatomy of baby brains: A review. *NeuroImage*, 185, 906–925.
- Li, R., Duan, C., & Zheng, S. (2020). MACU-Net semantic segmentation from high-resolution remote sensing images. *arXiv*. [Preprint] arXiv: 2007.13083.
- Liu, T., Li, H., Wong, K., Tarokh, A., Guo, L., & Wong, S. T. (2007). Brain tissue segmentation based on DTI data. *NeuroImage*, 38, 114–123.
- Long, J., Shelhamer, E., & Darrell, T. (2015). Fully convolutional networks for semantic segmentation. *IEEE Transactions on Pattern Analysis and Machine Intelligence*, 39, 640–651.
- Makropoulos, A., Counsell, S. J., & Rueckert, D. (2018). A review on automatic fetal and neonatal brain MRI segmentation. *NeuroImage*, 170, 231–248.
- Mostapha, M., & Styner, M. (2019). Role of deep learning in infant brain MRI analysis. *Magnetic Resonance Imaging*, 64, 171–189.
- Nie, D., Wang, L., Adeli, E., Lao, C., Lin, W., & Shen, D. (2019). 3-D fully convolutional networks for multimodal isointense infant brain image segmentation. *IEEE Transactions on Cybernetics*, 49, 1123–1136.
- Nie, D., Wang, L., Gao, Y., & Shen, D. (2016). Fully convolutional networks for multi-modality isointense infant brain image segmentation. *Proceedings IEEE international symposium on biomedical imaging 2016*, pp. 1342–1345.
- Ronneberger, O., Fischer, P., & Brox, T. (2015). U-net: Convolutional networks for biomedical image segmentation. *International conference on medical image computing and computer-assisted intervention*. Springer, pp. 234–241.
- Sanroma, G., Benkarim, O. M., Piella, G., Lekadir, K., Hahner, N., Eixarch, E., & Ballester, M. A. G. (2018). Learning to combine complementary segmentation methods for fetal and 6-month infant brain MRI segmentation. *Computerized Medical Imaging and Graphics*, 69, 52–59.
- Su, Z., Fang, L., Kang, W., Hu, D., Pietikäinen, M., & Liu, L. (2020). Dynamic group convolution for accelerating convolutional neural networks. *European conference on computer vision*. Springer, pp. 138–155.
- Sun, Y., Gao, K., Wu, Z., Li, G., Zong, X., Lei, Z., Wei, Y., Ma, J., Yang, X., & Feng, X. (2021). Multi-site infant brain segmentation algorithms: The iSeg-2019 challenge. *IEEE Transactions on Medical Imaging*, 40, 1363–1376.
- Wang, F., Lian, C., Wu, Z., Zhang, H., Li, T., Meng, Y., Wang, L., Lin, W., Shen, D., & Li, G. (2019). Developmental topography of cortical thickness during infancy. *Proceedings of the National Academy of Sciences*, 116, 15855–15860.
- Wang, L., Gao, Y., Shi, F., Li, G., Gilmore, J. H., Lin, W., & Shen, D. (2015). LINKS: Learning-based multi-source Integration framework for segmentation of infant brain images. *NeuroImage*, 108, 160–172.
- Wang, L., Li, G., Adeli, E., Liu, M., Wu, Z., Meng, Y., Lin, W., & Shen, D. (2018). Anatomy-guided joint tissue segmentation and topological correction for 6-month infant brain MRI with risk of autism. *Human Brain Mapping*, 39, 2609–2623.
- Wang, L., Li, G., Shi, F., Cao, X., Lian, C., Nie, D., Liu, M., Zhang, H., Li, G., Wu, Z., Lin, W., & Shen, D. (2018). Volume-based analysis of 6-month-old infant brain MRI for autism biomarker identification and early diagnosis. *Medical image computing and computer assisted intervention*. 11072, pp. 411–419.
- Wang, L., Nie, D., Li, G., Puybareau, E., Dolz, J., Zhang, Q., Wang, F., Xia, J., Wu, Z., Chen, J., Thung, K. H., Bui, T. D., Shin, J., Zeng, G., Zheng, G., Fonov, V. S., Doyle, A., Xu, Y., Moeskops, P., ... Shen, D. (2019). Benchmark on automatic 6-month-old infant brain segmentation algorithms: The iSeg-2017 challenge. *IEEE Transactions on Medical Imaging*, 38, 2219–2230.
- Wang, L., Shi, F., Gao, Y., Li, G., Gilmore, J. H., Lin, W., & Shen, D. (2014). Integration of sparse multi-modality representation and anatomical constraint for isointense infant brain MR image segmentation. *NeuroImage*, 89, 152–164.
- Wang, L., Shi, F., Yap, P.-T., Gilmore, J. H., Lin, W., & Shen, D. (2012). 4D multi-modality tissue segmentation of serial infant images. *PLoS One*, 7, e44596.
- Wang, Z., Zou, N., Shen, D., & Ji, S. (2020). Non-local U-Nets for biomedical image segmentation. *Proceedings of the AAAI Conference on Artificial Intelligence*, 34, 6315–6322.
- Wen, X., Zhang, H., Li, G., Liu, M., Yin, W., Lin, W., Zhang, J., & Shen, D. (2019). First-year development of modules and hubs in infant brain functional networks. *NeuroImage*, 185, 222–235.
- Xu, Y., Cao, M., Liao, X., Xia, M., Wang, X., Jeon, T., Ouyang, M., Chalak, L., Rollins, N., & Huang, H. (2019). Development and emergence of individual variability in the functional connectivity architecture of the pre-term human brain. *Cerebral Cortex*, 29, 4208–4222.
- Yushkevich, P. A., Piven, J., Hazlett, H. C., Smith, R. G., Ho, S., Gee, J. C., & Gerig, G. (2006). User-guided 3D active contour segmentation of anatomical structures: Significantly improved efficiency and reliability. *NeuroImage*, 31, 1116–1128.
- Zeng, G., & Zheng, G. (2018). Multi-stream 3D FCN with multi-scale deep supervision for multi-modality isointense infant brain MR image segmentation. *International symposium on biomedical imaging*, pp. 136–140.
- Zhang, J., Jiang, Z., Liu, D., Sun, Q., Hou, Y., & Liu, B. (2022). 3D asymmetric expectation-maximization attention network for brain tumor segmentation. *NMR in Biomedicine*, 35, e4657.
- Zhang, W., Li, R., Deng, H., Wang, L., Lin, W., Ji, S., & Shen, D. (2015). Deep convolutional neural networks for multi-modality isointense infant brain image segmentation. *NeuroImage*, 108, 214–224.
- Zhao, T., Xu, Y., & He, Y. (2019). Graph theoretical modeling of baby brain networks. *NeuroImage*, 185, 711–727.

How to cite this article: Zeng, Z., Zhao, T., Sun, L., Zhang, Y., Xia, M., Liao, X., Zhang, J., Shen, D., Wang, L., & He, Y. (2023). 3D-MASNet: 3D mixed-scale asymmetric convolutional segmentation network for 6-month-old infant brain MR images. *Human Brain Mapping*, 44(4), 1779–1792. <https://doi.org/10.1002/hbm.26174>